On the Limitations of Spectral Source Parameter Estimation for Minor and Microearthquakes

Stefano Parolai[*1] and Adrien Oth[2]

ABSTRACT

Reliable estimation of earthquake source parameters is fundamental to improve our understanding of earthquake source physics and for ground-motion modeling in seismic hazard assessment. Nowadays, methods traditionally used for investigating the source parameters of earthquakes with $M_w \geq 3$, such as spectral fitting or spectral ratio approaches, are also extensively applied to smaller magnitude events because of the increase in the number of stations and the more common borehole installations. However, when working with recordings of such minor and microearthquakes, significant limitations of the usable frequency range spanned by the spectra arise. At the lower end, signal-to-noise ratio constraints limit the usage of low frequencies, whereas at the upper end, the sampling rates of typical seismological networks as well as high-frequency attenuation can be limiting factors. In addition, earthquake source parameters determined from ground-motion spectra are known to exhibit potentially serious trade-offs, in particular the corner frequency and high-frequency attenuation. In this study, we go beyond the typical discussion of these trade-offs using simplistic spectral models by investigating the impact of the background wave propagation model on the source parameter trade-offs as well as its effect on the feasibility of obtaining useful source parameters by means of spectral fitting for minor and microevents. The analysis takes advantage of ad hoc simulated synthetic seismograms with well-defined underlying background propagation models and considers increasing complications in these models (intrinsic and scattering attenuation). The results show that with given realistic background models and usable frequency bands, the source parameter estimation for minor and microevents can be significantly biased, and not surprisingly, this bias is mainly affecting the estimation of the corner frequency. We highlight the inherent limitations of joint spectral fitting approaches for the determination of source parameters from minor and microearthquakes, which should always be viewed with great caution when physically interpreted.

KEY POINTS

- We investigate the reliability of spectral source parameters estimated for minor and microearthquakes.
- Synthetic seismograms calculated for various background wave propagation models are considered.
- Source parameters from spectral fitting of minor and microearthquakes should be interpreted with caution.

INTRODUCTION

Reliable estimation of earthquake source parameters is of major importance for a better understanding of the physics of earthquakes and for improving the assessment of seismic hazard. Over the past decades, the increase in the number and quality of seismic stations makes it possible to obtain recordings for smaller and smaller magnitude events, allowing us to improve the completeness of earthquake catalogs and investigate the scaling properties of the earthquake source. This development has been largely driven by the issues encountered with the occurrence of anthropogenic seismicity (e.g., Brown and Ge, 2018; Foulger *et al.*, 2018; Buijze *et al.*, 2019; Schultz *et al.*, 2020; and references therein), massively boosting the interest of the scientific community and practitioners in minor and microearthquakes ($M_w \leq 2$).

As a result, methods traditionally used for investigating the source parameters of earthquakes with $M_w \geq 3$, such as spectral fitting or spectral ratio approaches, have now also been extensively applied to smaller magnitude events (e.g., Jost *et al.*, 1998; Kwiatek *et al.*, 2014; Zollo *et al.*, 2014; Huang *et al.*, 2019; Moratto *et al.*, 2019; Klinger and Werner, 2022).

1. Istituto Nazionale di Oceanografia e di Geofisica Sperimentale—OGS, Sgonico, Italy, https://orcid.org/0000-0002-9084-7488 (SP); 2. European Center for Geodynamics and Seismology, Walferdange, Luxembourg, https://orcid.org/0000-0003-4859-6504 (AO)

*Corresponding author: sparolai@ogs.it

Cite this article as Parolai, S., and A. Oth (2022). On the Limitations of Spectral Source Parameter Estimation for Minor and Microearthquakes, *Bull. Seismol. Soc. Am.* **XX**, 1–12, doi: 10.1785/0120220050

However, the usable frequency range spanned by the spectra of such small earthquake recordings is typically limited at the lower end by signal-to-noise-ratio constraints (to frequencies typically well above 1 Hz depending on event size), whereas at the upper end, it is often hampered by the sampling rate typically adopted by seismological networks (100 or 200 samples per second), and even if significantly higher sampling rates are used, high-frequency attenuation effects and instrument response issues may be a severely limiting factor (Klinger and Werner, 2022). For magnitudes <1, the corner frequency can approach or overstep the aliasing frequency, and the signal-to-noise level might be low. However, the source pulse function of events with magnitudes around 2 (because of the longer duration) might already be wide enough to be significantly biased by arrivals because of scattering in the near-surface propagation (having similar frequency content and amplitude). In these conditions, reliable estimation of the source parameters (and in particular of the stress drop) might be problematic.

It is also well known that spectral estimation of earthquake source parameters is subject to significant trade-offs between the main parameters of relevance, in particular the corner frequency and the high-frequency spectral decay, typically parameterized in terms of attenuation parameter t^* (respectively Q) or kappa (Chen and Abercrombie, 2020). Ide *et al.* (2003) for instance showed that even for deep borehole records, spectral fitting using a standard omega-square model with the assumption of constant Q led to significantly lower corner frequency estimates compared with spectral ratio results, thus showing that path effects can contaminate measurements of earthquake source parameters even in deep borehole measurements. Ko *et al.* (2012) highlight the trade-off between t^* and f_c using a synthetic data test. Although t^* and f_c have in principle different contributions to the spectral shape, their effects can be difficult to distinguish in the presence of noise. Supino *et al.* (2019) introduced a probabilistic framework to better quantify the uncertainties and trade-offs arising during joint spectral fitting to retrieve earthquake source parameter estimates. Chen and Abercrombie (2020) provide a detailed investigation of the resolution limit of well-resolved corner frequencies with respect to the frequency bandwidth covered by the data (i.e., maximum frequency) based on a comparative analysis between joint spectral fitting of individual spectra to determine the relevant parameters and a stacking approach carried out on simple synthetic spectra (calculated assuming an omega-square source model and a given level of noise contamination) and a dataset of fluid-induced earthquakes near Guthrie, Oklahoma. One of their key findings is that corner frequencies <25% of the maximum usable frequency can be well recovered by joint spectral fitting, whereas the recovery of corner frequencies >40% of the maximum usable frequency strongly depend on signal-to-noise conditions and station distribution.

For these reasons, whenever possible, more refined source parameter estimation approaches, usually based on spectral ratios with appropriate empirical Green's functions (e.g., Kwiatek *et al.*, 2014), stacking or generalized inversion approaches of large datasets (e.g., Goertz-Allmann *et al.*, 2011; Picozzi *et al.*, 2017; Chen and Abercrombie, 2020), are preferred for robust source parameter estimation. Nonetheless, in many cases and especially when minor or microearthquakes are the target of the investigation, these techniques cannot be easily applied, and direct joint spectral estimation approaches remain the only possibility to potentially gain insights into their source parameters.

Although the trade-offs affecting spectral estimation of earthquake source parameters are thus nothing new, the discussion of these in the literature typically touches on the demonstration of their sheer existence and their (qualitative) effect or the resolution limits in terms of synthetic spectra calculated from simple parametric models. In this study, we specifically focus instead on investigating the impact of the background propagation model on the source parameter trade-offs and its effect on the feasibility of obtaining useful source parameters by means of spectral fitting for minor and microevents. The analysis takes advantage of ad-hoc simulated synthetic seismograms with well-defined underlying background propagation models and considers increasing complications in these models. It thus allows for an evaluation of the influence of the crustal heterogeneities and the material characteristics on the source parameter estimation. In a first step, the numerical simulations are described. Second, the analysis is carried out on a selected significant number of examples. Finally, the results are discussed with particular attention to their implication for the reliability of seismological studies on such minor or microseismic events.

SYNTHETIC SEISMOGRAMS CALCULATION

The synthetic seismograms are calculated using a semianalytical method that consists of an improved Thompson–Haskell propagator matrix algorithm (Wang, 1999) that avoids numerical instabilities between incident waves from the source at each layer interface using an orthonormalization approach.

The source function for the numerical simulation is given by a Brune source model (Brune, 1970, 1971). The seismic moment is estimated from the considered moment magnitude M_w using the relation (Hanks and Kanamori, 1979)

$$M_0 = 10^{1.5(M_w+10.7)}, \quad (1)$$

whereas the stress drop $\Delta\sigma$ is fixed to 1 MPa. This value was exemplarily chosen consistently to the average value depicted in figure 2 of Blanke *et al.* (2021), who collected data from different experiments. The hypocenter is always located at 10 km depth. Synthetics are calculated for an epicentral distance of 15 and 25 km orthogonally to a vertical strike slip rupture, with a sampling rate of 200 samples per second.

Different propagation models are considered starting from two basic configurations:

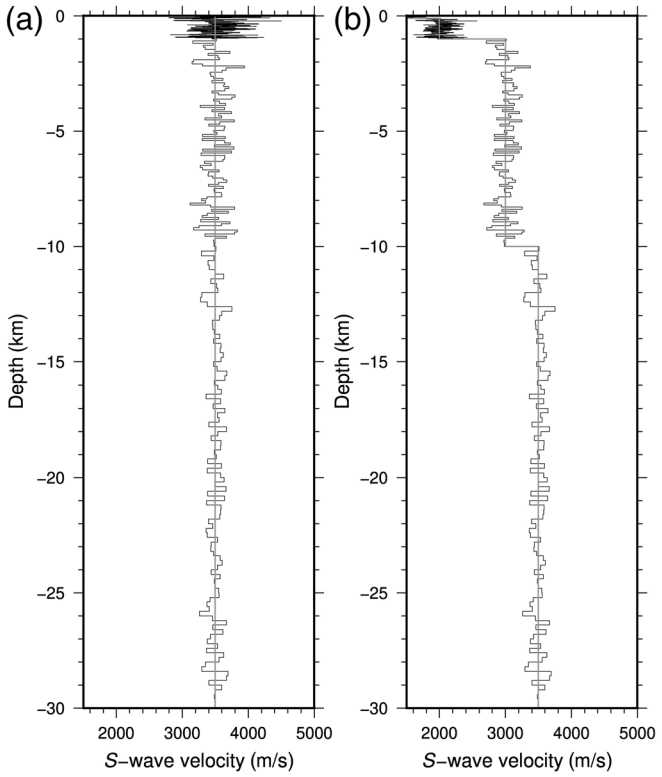

Figure 1. Velocity models setup. (a) M1-type models. (b) M2-type models.

- A homogeneous half-space ($V_P = 6.0\,\mathrm{km/s}$, $V_S = 3.5\,\mathrm{km/s}$), denoted as model **M1**
- A four-layer crustal (plus half-space) model **M2** organized as shown in Table 1.

Calculations are carried out considering the propagation of seismic wave in a nearly elastic model **M1e** and **M2e**, with *Qs* set equal to 9000, irrespective of depth. Moreover, models including intrinsic attenuation (**M1q** and **M2q**) are also considered. In the former of these two models, *Qs* was set equal to 300, whereas in the latter, *Qs* was fixed to 150, 200, 300, and 350 from the shallowest to the deepest layer.

To consider the effect of crustal heterogeneities, the layers (for both **M1** and **M2** model sets) have been further subdivided in smaller units with travel-time fluctuations. To this end, the uppermost 100 m were subdivided in 26 layers with 4 m thickness, the depth range between 100 m and 1 km in 100 layers with a thickness of 9 m, the depth range between 1 and 10 km in 100 layers with a thickness of 90 m, and the depth range between 10 and 30 km in 100 layers with a thickness of 200 m. The travel time within each of these layers is perturbed randomly (similar to Parolai, 2018) but with the constraint that the total travel time for the vertical propagation in the whole model (in case of **M1**) or for each layer (in the case of **M2**) is kept constant. Larger fluctuations (as well as smaller heterogeneities) are allowed for the shallowest

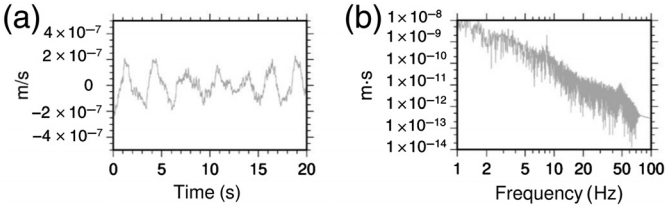

Figure 2. (a) Seismic noise time series. (b) Fourier spectrum of the seismic noise time series in displacement.

TABLE 1
Four Layer Model Velocity Parameterization

Thickness (km)	*P*-Wave Velocity V_P (km/s)	*S*-Wave Velocity V_S (km/s)
0.1	2.6	1.5
0.9	3.464	2.0
9	5.196	3.0
20	6.0	3.5
Half-space	6.0	3.5

depth (standard deviation equal to 0.15, 0.10, 0.05, 0.03 of the travel time) according to evidence from boreholes investigation (Raub *et al.*, 2016). In view of the frequency range computed in this simulation and the considered velocity models and thicknesses of the layers, these later phases that will appear in the synthetic seismograms are mainly caused by Rayleigh and Mie (resonance) scattering regimes (Wu and Aki, 1988). The obtained models, when elastic, are named **M1e_s** and **M2e_s**, whereas when the intrinsic attenuation is also considered, they are named **M1q_s** and **M2q_s**. Figure 1 summarizes the velocity structures that have been considered in the analysis.

Finally, real seismic noise recorded at one of the less noisy stations of the SMINO network (Bragato *et al.*, 2021) is added to the data (Fig. 2). This allows to investigate the possible limitation in the source parameters estimation in the optimal case of a low-noise environment.

RELIABILITY TEST IN THE SIMPLEST CASE

To validate the reliability of the results obtained by the procedure, the transverse component seismogram of an $M_w = 2$ event has been generated using the **M1** model, that is, the simplest case in which the uncertainties in travel times and *Q* averaging that could affect the spectral fitting are ruled out. Considering equation (1) and the relationships (Brune, 1970)

$$f_c = \frac{2.34Vc}{2\pi\delta} \text{ with } \delta = \left(\frac{7M_0}{16\Delta\sigma}\right), \tag{2}$$

in which M_0 is the seismic moment; Vc is the *S*-wave velocity (3500 m/s); $\Delta\sigma$ is the stress drop (fixed as mentioned earlier to

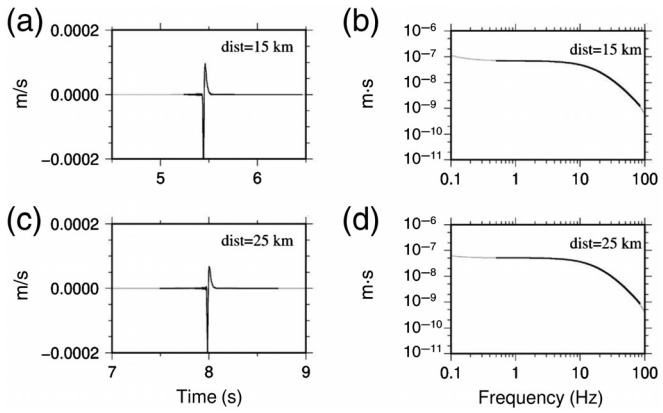

Figure 3. (a,c) Transverse component synthetic seismograms (gray line), calculated at (a) 15 km and (c) 25 km epicentral distance. The black line indicates the selected part of the signal used for the Fourier spectra calculations. (b,d) Fourier spectra of the transverse component seismograms, calculated at (b) 15 km and (d) 25 km epicentral distance. The black line indicates the frequencies used in the spectral fitting procedure.

1 MPa); and δ is the source dimension, a corner frequency f_c equal to 16.5 Hz is expected. Considering that a window length of 1.225 s around the *S*-wave pulse was selected to calculate the Fourier spectra of the recordings and the used sampling rate, the f_c results to be well inside the usable frequency band. The window length was selected, similar to the standard practice when analyzing real data, as a compromise between the minimum frequency that can be used and, considering the following analysis, the amount of secondary and scattered arrivals affecting the recordings. Figure 3 shows the calculated signals (in velocity) and the corresponding Fourier spectra in displacement.

The spectral fit was carried out using a Brune source model:

$$Bc(f) = \frac{\Omega}{1 + \left(\frac{f}{f_c}\right)^2}, \tag{3}$$

$$\Omega = \frac{2RM_0}{4\pi\rho V c^3 r}, \tag{4}$$

in which r is the hypocentral distance, R is the average radiation pattern (fixed here to 0.6), and ρ is the density (2800 kg/m^3 both for the generation of the data and the spectral fitting).

Furthermore, to account for the effect of anelastic attenuation, a frequency-independent quality factor Q is considered in a frequency-dependent attenuation $e^{\frac{-\pi f t}{Q}}$, taken into account in the spectral fitting procedure subsequently, in which t is the travel time. Although t was calculated considering the source-to-site distance and the velocity of the **M1** model, the Q was one of the unknown parameters to be estimated in the spectral fitting procedure.

The spectral fit was carried out in the 0.5–85 Hz frequency band by means of a grid-search procedure. However, in real cases, the signal-to-noise ratio can further limit the exploitable frequency band, particularly at sites where the level of noise is higher than the very low one reported in Figure 2. The misfit was estimated as the L2 norm of the differences between the logarithm of the observed and calculated spectral amplitudes. M_0 was chosen to range between 1×10^{11} N · m and 8.9×10^{13} N · m in 60 equally spaced in logarithmic scale steps. f_c was tested in the 1–41 Hz range for 80 equally spaced values. Thirty Q values, with a step of 500, ranging from 500 to 15,000, were considered. All the other parameter values were kept as identical to the source wavelet simulation.

Figure 3b,d shows that an excellent fit of the spectra is obtained. Figure 4 shows the misfit values versus the grid-search parameters on slices cut in correspondence of the minimum misfit solution (white star) when the seismogram at 15 km epicentral distance is considered. The black star indicates the real values used for the synthetic seismogram calculation. The results indicate that in a nearly elastic model and for the short distances considered, the solution is virtually insensitive to the Q factor, although the best solution is obtained for a value of 1500. Despite some level of trade-off between the parameters, M_0 and f_c are reliably estimated with small differences in the order of 30% and 9% with respect to the real values, respectively. Discrepancies between the M_0 estimate and the real value can arise from the finite step of the grid-search procedure (this might be diminished using smaller steps) and the differences between the actual radiation pattern and the adopted simple constant value for its representation in the spectral fitting. These differences might be considered as a reference value for the following analysis.

RESULTS FOR DIFFERENT PROPAGATION MODELS

In the following, first the results obtained for different levels of complexity of the propagation model are shown for an $M_w = 1$ event. Second, the results obtained for an $M_w = 0.5$ and an $M_w = 2$ event in the case of only the most complicated crustal model are shown for completeness of information and to draw comprehensive conclusions about the analysis.

M_w 1 earthquake

The synthetic seismograms were first calculated for the **M1e** model. In this case, the f_c of the event is at 52.25 Hz, which is still inside the exploitable frequency band but significantly closer to the upper limit. f_c was tested in the 35–75 Hz frequency range, and the spectral fitting was carried out in the 4.5–85 Hz range, where the signal-to-noise ratio is >3 (see also Fig. 2). In fact, the added seismic noise, being selected from a high-quality seismic station without significant anthropogenic high-frequency noise components, is mainly affecting low frequencies, therefore limiting the usable frequency band to frequencies >4.5 Hz. In case the seismic noise recorded from less quiet

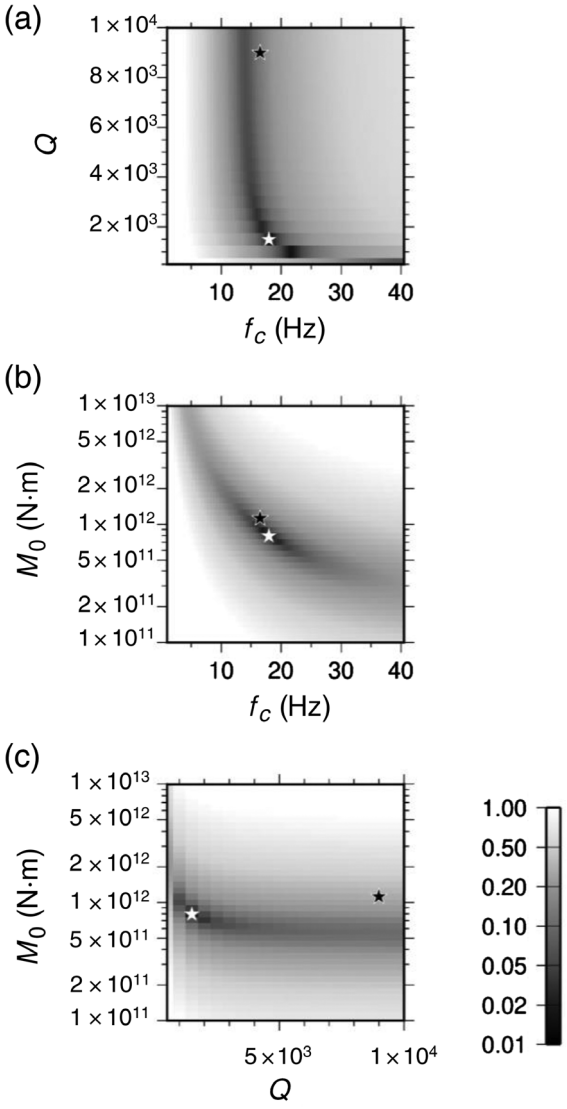

Figure 4. Misfit value on planes crossing the best-fit solution. The white star indicates the minimum misfit solution, and the black star depicts the real values used for the synthetic seismogram calculation. (a) Visualization on the $Q - f_c$ plane, (b) visualization on the $M_0 - f_c$ plane, and (c) visualization on the $M_0 - Q$ plane.

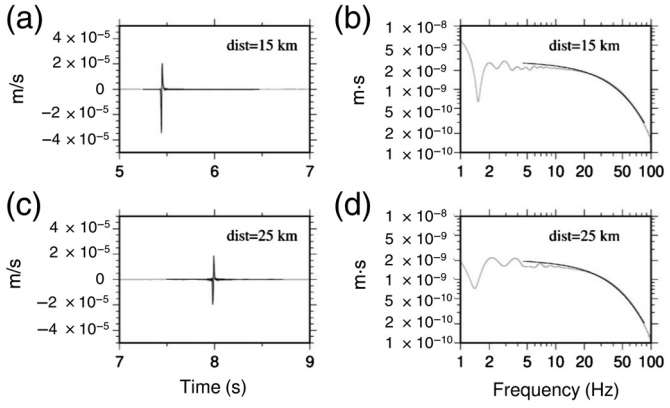

Figure 5. Same as Figure 3 but for an M_w 1 event and considering the **M1e** model.

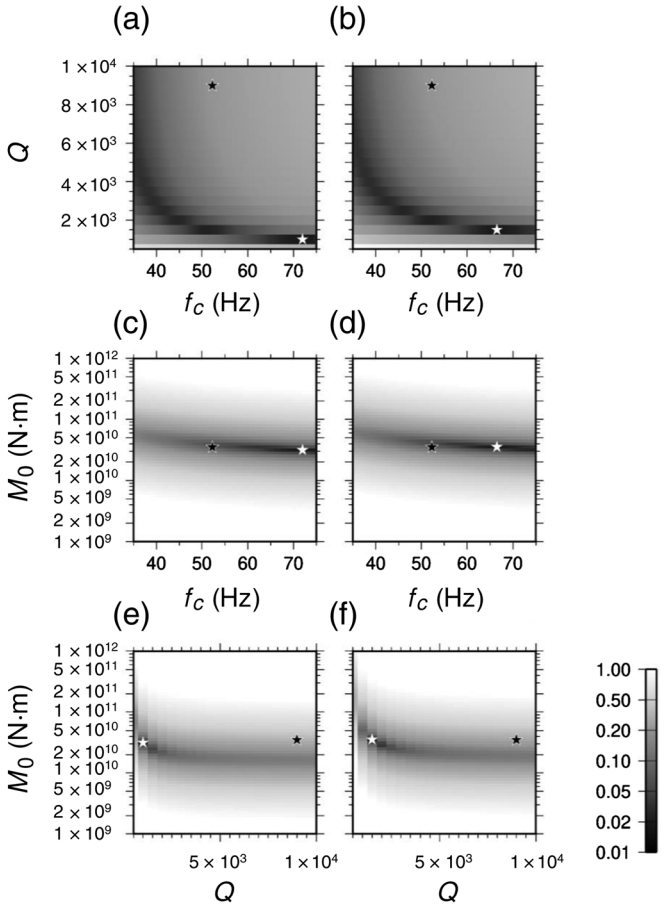

Figure 6. Misfit value on planes crossing the best-fit solution for an M_w 1 event and considering the **M1e** model. The white star indicates the minimum misfit solution, and the black star depicts the real values used for the synthetic seismogram calculation. (a,c,e) Results for epicentral distance of 15 km: (a) visualization on the $Q - f_c$ plane, (c) visualization on the $M_0 - f_c$ plane, and (e) visualization on the $M_0 - Q$ plane. (b,d,f) Results for epicentral distance of 25 km: (b) visualization on the $Q - f_c$ plane, (d) visualization on the $M_0 - f_c$ plane, and (f) visualization on the $M_0 - Q$ plane.

stations would have been added, the signal-to-noise ratio would have dropped also in the high-frequency range. Figure 5 shows that a very good fit of the spectra can be obtained.

The results of the spectral fitting (Fig. 6) show that even in this simple case, the limitation because of using a narrow frequency band above the corner frequency, and therefore to correctly capture the high-frequency decay of the spectrum, leads to an increased uncertainty (with respect the previous case) in the estimation of f_c. As in the previous case, the grid-search results in a best estimation of Q at a relatively low value (1000 for the 15 km and 1500 for the 25 km distance) because larger Q values are not modifying the spectra significantly in the considered frequency range, and the spectral fit becomes

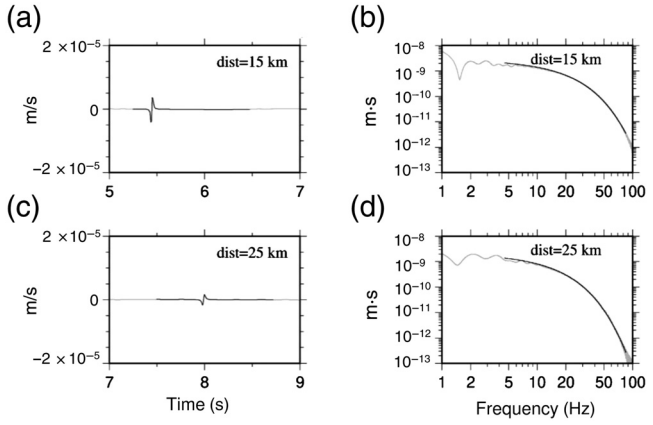

Figure 7. Same as Figure 3 but for an M_w 1 event and considering the **M1q** model. Note the different amplitude level and frequency content of the signals in the left panels.

insensitive to variations of Q at higher values. This in turn leads to a significant overestimation of f_c. M_0 is estimated within the expected uncertainty.

The results for the **M1q** model show that, again, a very good fit of the spectra is obtained (Fig. 7). The effect of having considered a Q factor in the simulation is obvious both in the time series (diminishing of the peak amplitude and widening of the pulse) and the spectra (stronger high-frequency decay).

In this case, both Q and M_0 were very satisfactorily retrieved (240 and 3.16 × 10^{10} N·m at 15 km distance; 260 and 3.55 × 10^{10} N·m at 25 km distance), whereas it is clear that f_c is poorly constrained, although the minimum misfit was obtained for values only 30% and 20% larger than the true value for the recordings at 15 km and 25 km, respectively (Fig. 8).

When the **M1e_s** model is adopted, the results show that scattering has a strong effect in diminishing the peak amplitude of ground motion and in increasing its duration because of later arrivals (Fig. 9). These later arrivals have an effect on the high-frequency spectrum for the short distance path but are affecting also the low-frequency range for the long (25 km) distance path. At 25 km distance, the signal is dominated by seismic noise <5 Hz.

Figure 10 shows that adding the heterogeneities effect renders the estimation of the Q entirely unreliable and leads to large uncertainties in the f_c assessment, although the latter is still estimated within 13% and 30% of the real value at 15 km and 25 km, respectively. M_0 is obtained within a factor 2.8 that would lead to an underestimation of 0.3 units in magnitude. The part of the uncertainty might arise from the attenuation correction based on the travel time estimated for the homogeneous model that might obviously be slightly different from the actual travel time for nonvertical propagation in the heterogeneous medium.

Combining both the anelastic and transmission effects in model **M1q_s** leads to synthetic signals where the amplitude

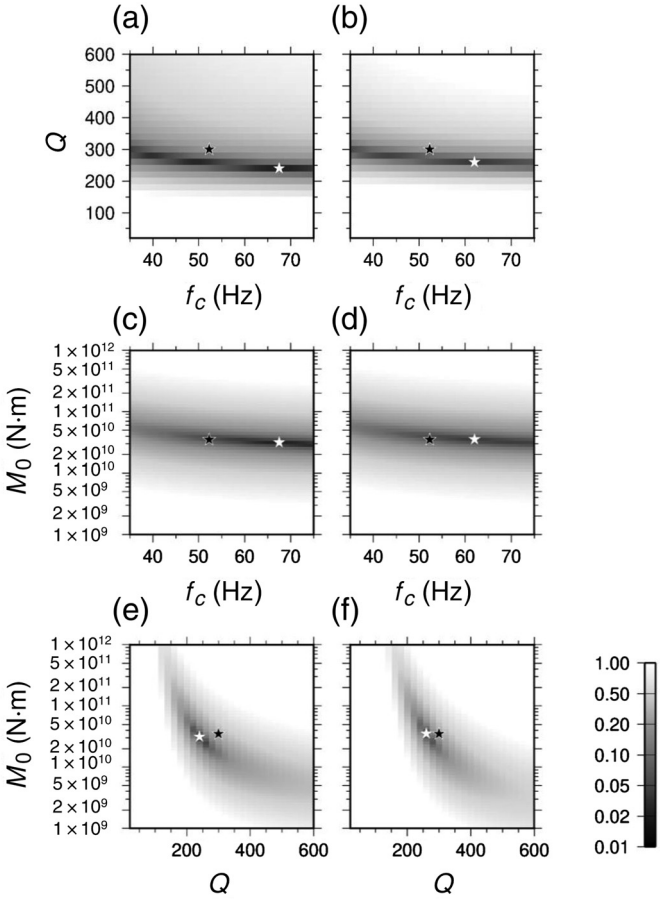

Figure 8. Misfit value on planes crossing the best-fit solution for an M_w 1 event and considering the **M1q** model. The white star indicates the minimum misfit solution, and the black star depicts the real values used for the synthetic seismogram calculation. (a,c,e) results for epicentral distance of 15 km: (a) visualization on the $Q - f_c$ plane, (c) visualization on the $M_0 - f_c$ plane, (e) and visualization on the $M_0 - Q$ plane. (b,d,f) Results for epicentral distance of 25 km: (b) visualization on the $Q - f_c$ plane, (d) visualization on the $M_0 - f_c$ plane, (f) and visualization on the $M_0 - Q$ plane.

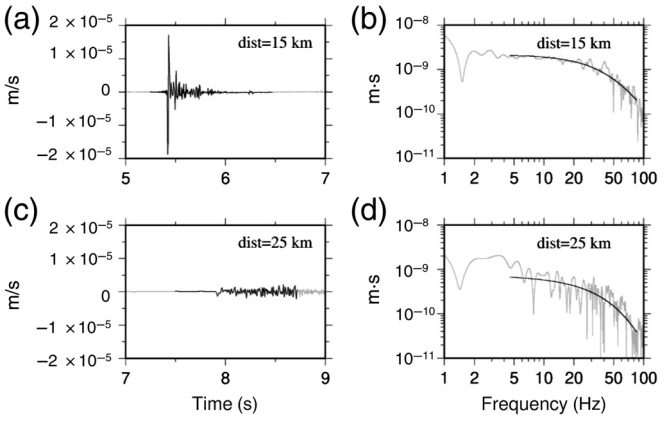

Figure 9. Same as Figure 3 but for an M_w 1 event and considering the **M1e_s** model. Note the different amplitude level and frequency content of the signals in the left panels.

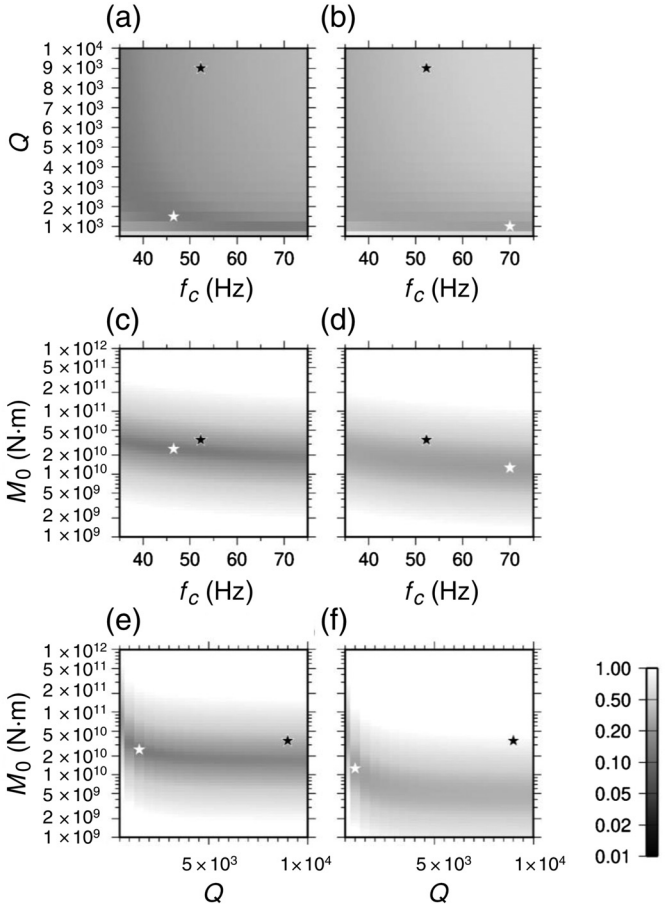

Figure 10. Misfit value on planes crossing the best-fit solution for an M_w 1 event and considering the **M1e_s** model. The white star indicates the minimum misfit solution, and the black star depicts the real values used for the synthetic seismogram calculation. (a,c,e) Results for epicentral distance of 15 km: (a) visualization on the $Q - f_c$ plane, (c) visualization on the $M_0 - f_c$ plane, (e) and visualization on the $M_0 - Q$ plane. (b,d,f) Results for epicentral distance of 25 km: (b) visualization on the $Q - f_c$ plane, (d) visualization on the $M_0 - f_c$ plane, and (f) visualization on the $M_0 - Q$ plane.

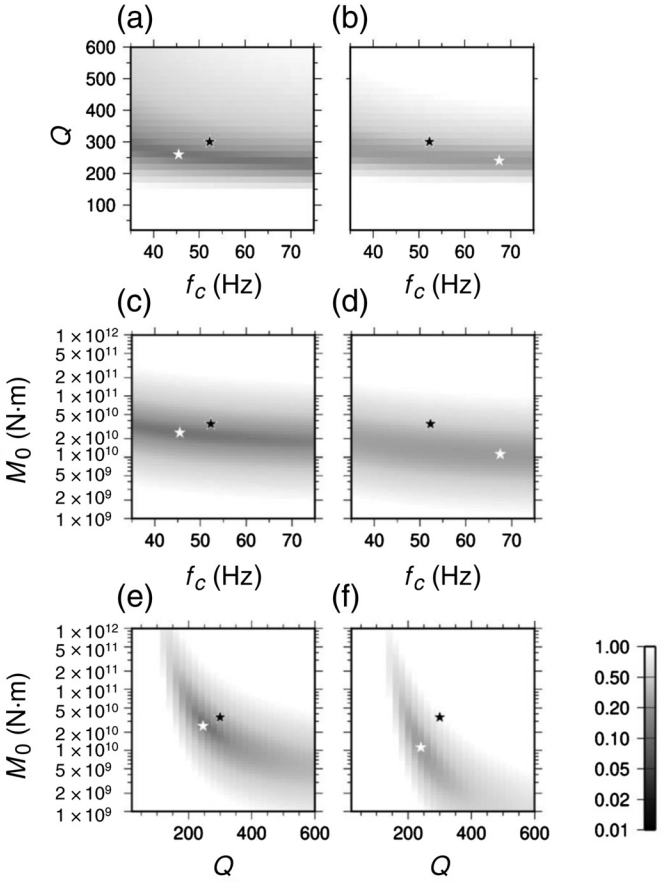

Figure 12. Misfit value on planes crossing the best-fit solution for an M_w 1 event and considering the **M1q_s** model. The white star indicates the minimum misfit solution, and the black star depicts the real values used for the synthetic seismogram calculation. (a,c,e) Results for epicentral distance of 15 km: (a) visualization on the $Q - f_c$ plane, (c) visualization on the $M_0 - f_c$ plane, and (e) visualization on the $M_0 - Q$ plane. (b,d,f) Results for epicentral distance of 25 km: (b) visualization on the $Q - f_c$ plane, (d) visualization on the $M_0 - f_c$ plane, and (f) visualization on the $M_0 - Q$ plane.

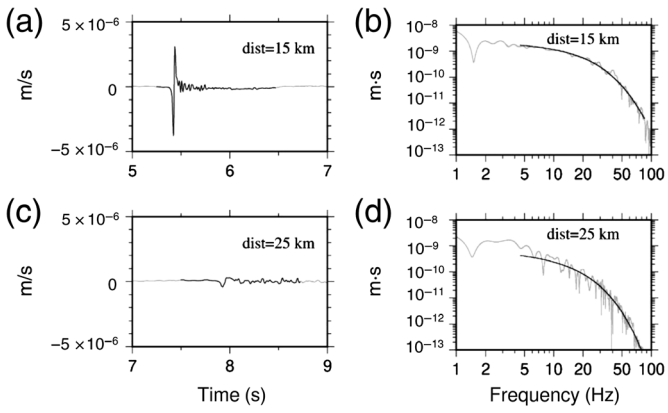

Figure 11. Same as Figure 3 but for an M_w 1 event and considering the **M1q_s** model. Note the different amplitude level and frequency content of the signals in the left panels.

of the scattered phases is strongly attenuated but still significant, particularly at 15 km distance (Fig. 11).

This results in a fair estimation of the source parameters and Q for the 15 km epicentral distance. Increasing the epicentral distance leads to a poor estimation of all parameters (with M_0 underestimated by a factor 3), particularly f_c is with a large uncertainty (Fig. 12).

Finally, we also show the results obtained by considering the layered model **M2**. Because the effect of layering adopted in this work was observed to only have a small influence on the calculated wavefield in comparison with the **M1** model, the results are shown only for the most complex model (**M2q_s**). For this model, the theoretical travel time used in the grid-search inversion was estimated considering the hypocentral distance and an averaged velocity form the source position to the surface, as generally done for real-data analysis. The reference quality factor for the comparison was estimated considering the weighted average

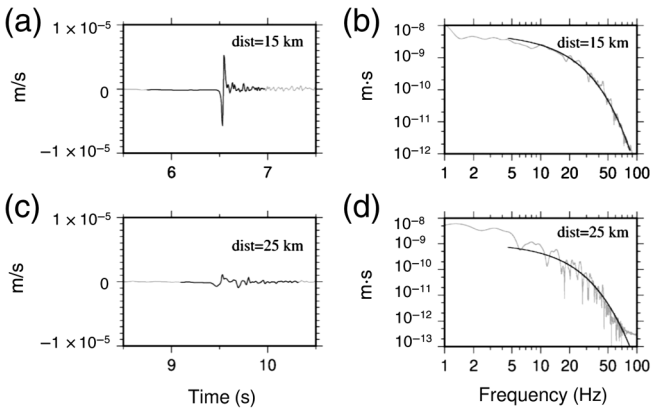

Figure 13. Same as Figure 3 but for an M_w 1 event and considering the **M2q_s** model. Note the different amplitude level and frequency content of the signals in the left panels.

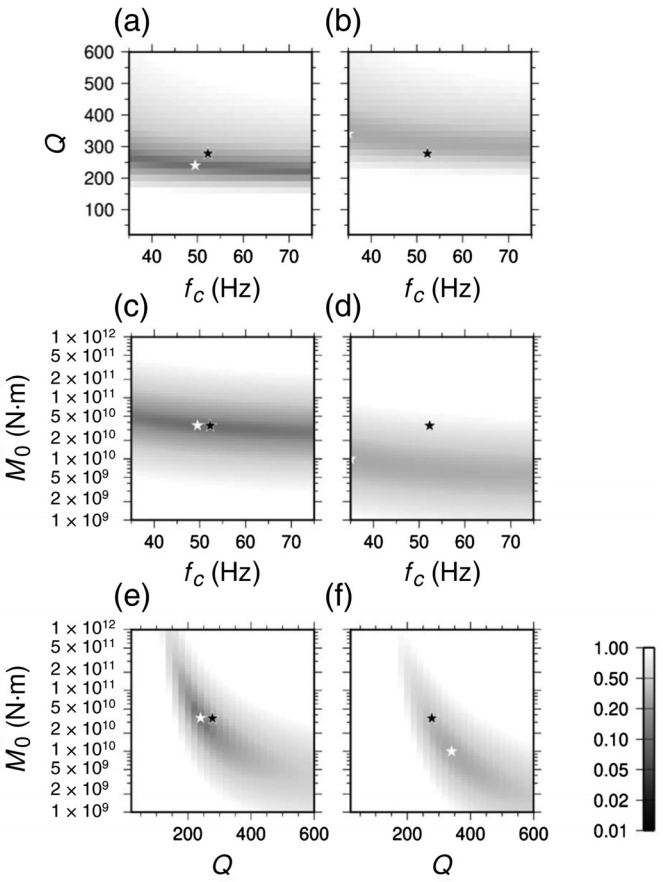

Figure 14. Misfit on planes crossing the best-fit solution for an M_w 1 event and considering the **M2q_s** model. The white star indicates the minimum misfit solution, and the black star depicts the real values used for the synthetic seismogram calculation. (a,c,e) Results for epicentral distance of 15 km: (a) visualization on the $Q - f_c$ plane, (c) visualization on the $M_0 - f_c$ plane, and (e) visualization on the $M_0 - Q$ plane. (b,d,f) Results for epicentral distance of 25 km: (b) visualization on the $Q - f_c$ plane, (d) visualization on the $M_0 - f_c$ plane, and (f) visualization on the $M_0 - Q$ plane.

of the quality factor using the vertical travel time as weight. All these choices, which we stress are similar to what is done generally when dealing with real data, can, of course, generate some discrepancies between the reference and the estimated values of the source parameters.

Figure 13 shows that for the 15 km distance, a very good spectral fit can be obtained, but the quality is decreasing with increasing hypocentral distance because of a larger effect of the complexity of the medium and the poorer signal-to-noise ratio in the low-frequency range.

Figure 14 confirms that combining intrinsic attenuation and transmission effects results in a fair estimation of the source parameters and Q for the 15 km epicentral distance, although the poor capability in constraining the corner frequency is obvious. Increasing the epicentral distance leads to very uncertain estimation of all parameters (with M_0 underestimated by a factor 3.5), and in particular, f_c is determined at the minimum value tested in the grid search.

M_w 0.5 earthquake

Having discussed with the earlier example the contribution of the different attenuation mechanisms (intrinsic vs. scattering) to the spectral fitting results, for the $M_w = 0.5$ case, we only show the results obtained while considering the **M2q_s** model. In this case, the corner frequency f_c of the event is at 92.9 Hz, which is at the very end of the potentially exploitable frequency band. At low and high frequencies, the signal-to-noise ratio can be small or equal to 1 (see Fig. 2). Therefore, the spectral fitting was carried out between 4.5–85 Hz and 4.5–70 Hz for the 15 km and 25 km epicentral distance, respectively. f_c was tested in the 70–110 Hz frequency band to generate the spectra in the grid-search procedure, restricting then the frequency band for comparison with the values indicated previously. The latter value, although above the Nyquist frequency, is only used to generate the theoretical spectra within the exploitable frequency band.

The effect of the low-frequency noise is now becoming clearer both in the time series and in the spectra (Fig. 15). However, a satisfactory and sufficient fit is still obtained for the shortest and the longest analyzed distances, respectively. The results (Fig. 16) show that a fair estimation of the seismic moment and Q can still be obtained at 15 km epicentral distance. The assessment of f_c is highly uncertain, although it is accidentally estimated at 10% of its real value. When the distance is increasing, the fit quality is worsening, uncertainties are increasing, and M_0 tends to be underestimated.

M_w 2.0 earthquake

The results obtained by considering an $M_w = 2$ event ($f_c = 16.25$ Hz) with model **M2q_s** are shown in Figures 17 and 18. In this case, f_c was tested in the 1–41 Hz frequency range, and the spectral fitting was carried out in the 1–85 Hz frequency

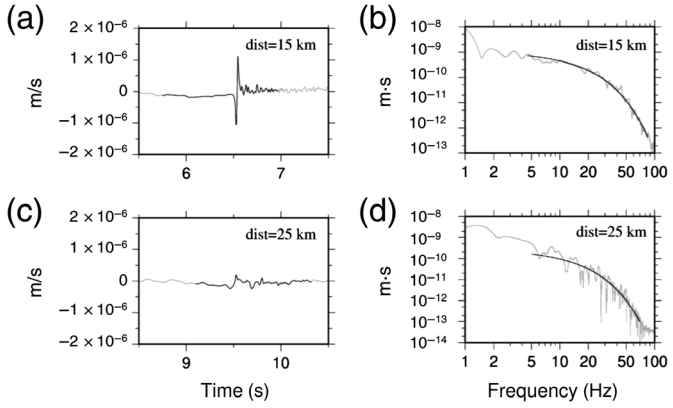

Figure 15. Same as Figure 3 but for an M_w 0.5 event and considering the **M2q_s** model.

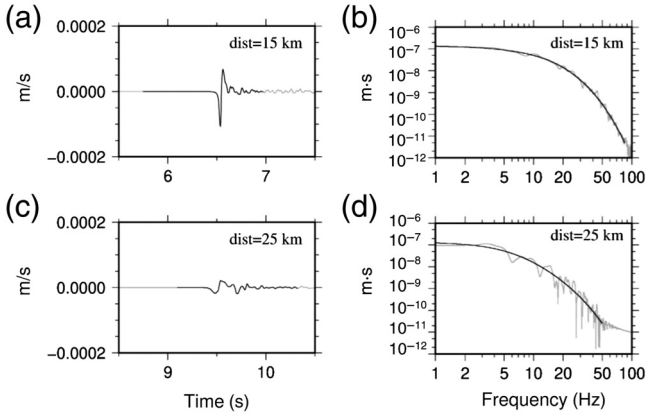

Figure 17. Same as Figure 3 but for an M_w 2.0 event and considering the **M2q_s** model.

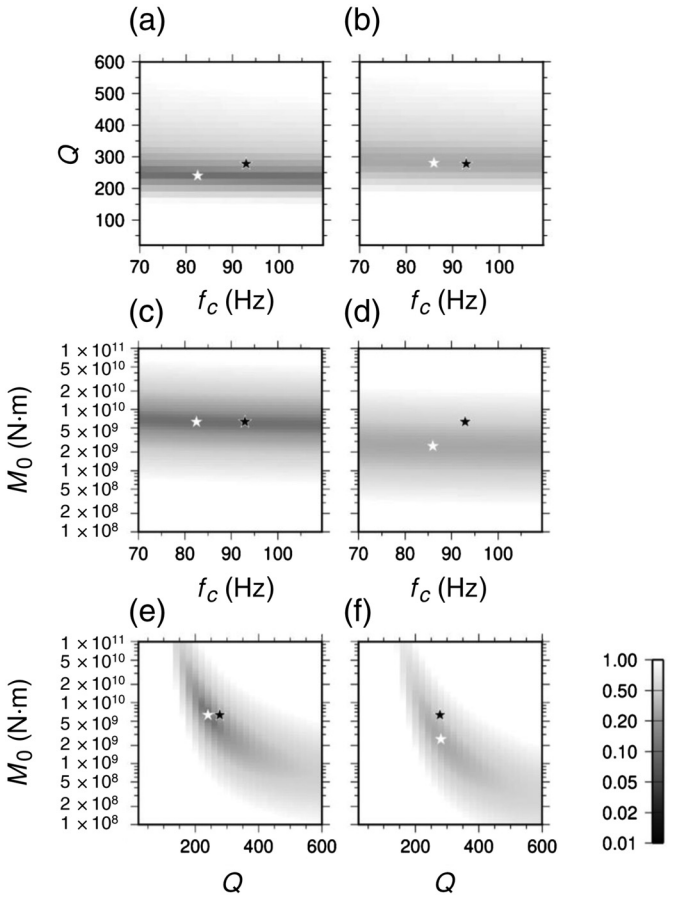

Figure 16. Misfit value on planes crossing the best-fit solution for an M_w 0.5 event and considering the **M2q_s** model. The white star indicates the minimum misfit solution, and the black star depicts the real values used for the synthetic seismogram calculation. (a,c,e) Results for epicentral distance of 15 km: (a) visualization on the $Q - f_c$ plane, (c) visualization on the $M_0 - f_c$ plane, and (e) visualization on the $M_0 - Q$ plane. (b,d,f) Results for epicentral distance of 25 km: (b) visualization on the $Q - f_c$ plane, (d) visualization on the $M_0 - f_c$ plane, and (f) visualization on the $M_0 - Q$ plane.

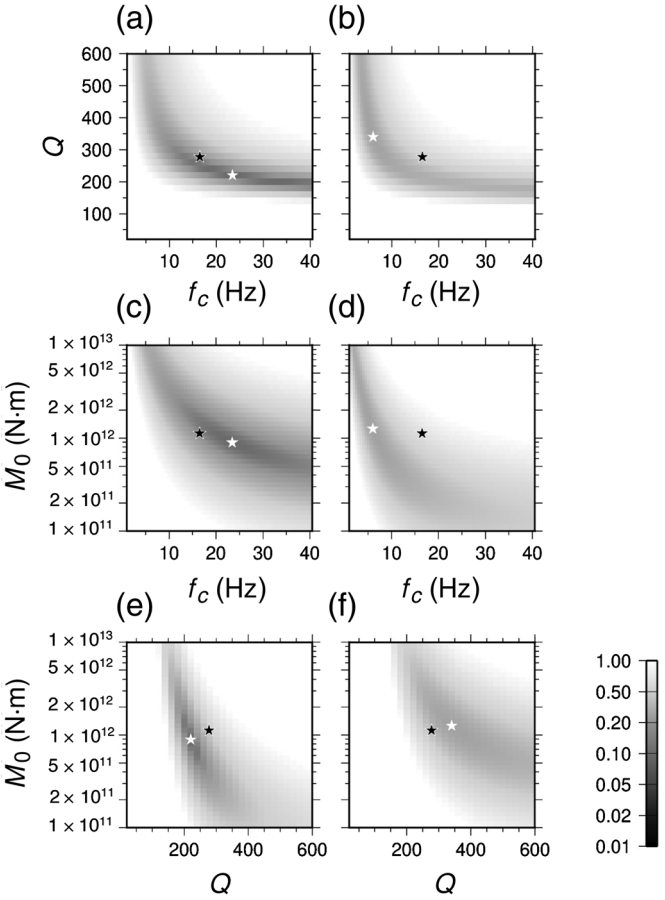

Figure 18. Misfit value on planes crossing the best-fit solution for an M_w 2.0 event and considering the **M2q_s** model. The white star indicates the minimum misfit solution, and the black star depicts the real values used for the synthetic seismogram calculation. (a,c,e) Results for epicentral distance of 15 km: (a) visualization on the $Q - f_c$ plane, (c) visualization on the $M_0 - f_c$ plane, and (e) visualization on the $M_0 - Q$ plane. (b,d,f) Results for epicentral distance of 25 km: (b) visualization on the $Q - f_c$ plane, (d) visualization on the $M_0 - f_c$ plane, and (f) visualization on the $M_0 - Q$ plane.

band. Clearly, the first arrival (because of a longer duration of the source pulse) is already mixed with later scattered arrivals. However, the presence of the considered heterogeneities is not affecting the excellent fit of the spectrum, particularly at 15 km epicentral distance.

The seismic moment and the Q are well estimated, especially at short distances, but the corner frequency still appears as the most uncertain parameter and is overestimated by ~40%. A clear trade-off in the parameter estimation (in particular between Q and f_c but also between M_0 and f_c) is obvious. Similar results are obtained for the 25 km epicentral distance but with a worsening of the fit function, leading to an estimation of f_c 2.75 times smaller than the imposed one.

DISCUSSION AND CONCLUSIONS

The results of the different cases considered here highlight the challenges encountered in the determination of reliable source parameters from the observed ground-motion spectra of minor and microearthquakes using joint spectral fitting approaches to simultaneously determine M_0, f_c, and Q estimates. These results might also be extended to the spectral fitting carried out on the generalized inversion technique (GIT) source spectra (e.g., Anderson, 1986; Castro *et al.*, 1990) because they are obtained using simplified attenuation models. Furthermore, when the number of stations used in the inversion is also limited (or poorly distributed), it cannot be guaranteed that the estimated average source model is not biased by propagation effects (e.g., Shible *et al.*, 2022).

Although in this study we considered only a fixed source depth (10 km), the results can also be considered representative for shallower sources in the considered epicentral distance range (the hypocentral distance changes would explain a 40% amplitude reduction in the most extreme case). Furthermore, when dealing, for example, with shallow induced earthquakes, the large seismic noise at the recording sites (much larger than the small one used in this study) would counteract the larger expected spectral amplitudes, limiting the exploitable frequency bandwidth.

When considering $M_w = 1$ earthquakes with corner frequencies well inside the usable frequency band, the Q-value of the nearly elastic case **M1e** (i.e., very high Q-value) cannot be captured because of very limited changes in the spectral shape for Q-values above a given threshold and the trade-off with f_c. The inclusion of scattering in model **M1e_s** completely removes the already limited sensitivity of the spectral fitting to Q. This shows that, even if a more complicated (e.g., frequency-dependent) Q could be considered in the spectral fitting, the effects caused by the limited frequency bandwidth are prevailing.

When a reasonably low Q-value is chosen in the synthetics to include anelastic attenuation in the simulations (**M1q**), the Q-value can be reasonably well constrained (within a range of a few hundred percent) even though some sensitivity is lost with the additional inclusion of scattering (**M1q_s**). Interestingly though, this better constraint on Q does not have a similar effect on the determination of f_c, which is in all cases very uncertain, with a clear tendency for overestimation in the models without scattering. When scattering is added, the corner frequency becomes very difficult to determine from the spectra, and a fit with "reasonable" value is in many cases more a matter of chance. In the models with anelastic attenuation, a more distinct trade-off curve between M_0 and Q develops, showing the influence of the spectral bandwidth limitation at low frequencies (in relation to the usable frequency band) for such small events related to signal-to-noise ratio constraints.

The effect of source-to-site distance also becomes evident from the cases studied, as one would obviously expect. Both the quality of the spectral fit and the retrievability of the source parameters diminish, with strongest effect in the propagation models including crustal heterogeneities leading to scattering. For the most complex (and realistic) model **M2q_s**, for instance, a reasonable estimate of Q and the source parameters can be obtained at 15 km epicentral distance, but an increase to 25 km epicentral distance has a strong impact, especially on f_c and Q, the quality of the spectral fit becoming far less sensitive to the variations of these.

The consideration of the case of an earthquake with $M_w = 0.5$ instead of $M_w = 1$ illustrates well the problematic when the corner frequency of the event is located toward the upper end of the usable frequency range, as also discussed by Chen and Abercrombie (2020). In this case, there is no trade-off curve between f_c and M_0 or between f_c and Q, but the spectral fit is entire insensitive to the chosen f_c variations in a reasonable band around the expected value. In contrast, for an event with $M_w = 2$ with a corner frequency <25% limit of the usable frequency range set by Chen and Abercrombie (2020), a clearly defined trade-off curve develops between the different fit parameters, and here the key aspect that drives the increase of the uncertainties becomes the source-to-site distance (Fig. 17).

Interestingly, there is no remarkable difference between the homogeneous (**M1** class) and layered (**M2** class) models, as briefly mentioned at the beginning, suggesting that typical layering assumptions of crustal structure and the related depth dependence of Q probably play a more limited role in defining the trade-offs between the spectral fit parameters compared with the average level of Q and the effect of structural heterogeneities. Of course, the layering effect might become more pronounced in the case of deeper events. Overall, corner frequency is the least constrained parameter in the joint spectral fitting approach, which by itself is a conclusion that does not come as a surprise (e.g., the fundamental work of Boore, 1986, regarding the effect of finite bandwidth).

Beyond a pure discussion of the trade-offs encountered in joint spectral fitting of individual ground-motion spectra for source parameter estimation as seen so far in the literature, our study highlights the inherent limitations of this approach linked to the propagation of the seismic waves through a

heterogeneous medium such as the Earth's crust. Although technically, in a given combination of instrumental characteristics, sampling rate, and ambient seismic noise conditions, it might be expected that the corner frequency of an earthquake of a given magnitude should be resolvable, the inherent effects of seismic-wave propagation may make the results of such a spectral fit guess work, particularly for earthquakes with smaller and smaller magnitudes and at larger source-to-site distances. Source parameters of minor and microearthquakes determined by joint spectral fitting approaches should therefore always be viewed with great caution when physically interpreted. This is also consistent with the results of Pennington *et al.* (2021), who observed that the absolute values of stress drop vary significantly when estimated by different methods.

It is worth remembering that both the intrinsic Q and the scattering Q are contributing to the total attenuation estimated empirically. Although the former is generally assumed to be frequency independent, the frequency dependence is related to the scattering (or transmission) part (e.g., Menke and Chen, 1984; Parolai *et al.*, 2022). This model is certainly valid when only the source pulse is considered.

However, when using a window of signal also including the later arrivals, the effect of scattering on the spectral shape (and on the total attenuation) might be mitigated (Parolai, 2018). In this study, and consistent with the kappa estimation generally carried out for the rock sites such as those simulated here—that is, assuming a frequency-independent Q—we adopted models with frequency-independent intrinsic Q in each layer for the generation of synthetics, and we left the scattering to add any possible frequency dependence to the total attenuation.

In the spectral fitting, we considered a frequency-independent Q (useful to highlight possible problems even in the simplest case with a homogeneous and elastic model, in which a frequency dependence should not appear). A comparison of Figures 5 and 6 (**M1_e**) and Figures 9 and 10 (**M1_e_s**) shows, as mentioned earlier, that the effect of this choice is certainly smaller than the effect of the bandwidth limitation. This observation is consistent with the results of Bethmann *et al.* (2012), who investigated borehole recordings of micro to minor magnitude events and concluded that a frequency-independent Q is sufficient to approximate the spectral shape.

Furthermore, using a frequency-dependent Q in the spectral fitting procedure might improve the fitting, but it would generate additional trade-off between the parameters (e.g., Drouet *et al.*, 2008; Shible *et al.*, 2022). This is obviously due to, for example, the fact that Q is included in an exponential term that interferes with the source spectral decay.

This study only focused on a few representative examples, allowing us to highlight the risk in overinterpretation of the source parameters estimation. A future more systematic study considering different crustal models, source depths, stress drops, and larger magnitude range might help in providing quantitative constraints on the bias in the parameters as a function of magnitude and location of the earthquakes. When dealing with real data, collected also by networks with stations in sedimentary basins, a simple 1D approximation for the correction of the recorded spectra may not be sufficient (e.g., Imperatori and Mai, 2012; Pitarka and Mellors, 2021), and a frequency-dependent Q might help in improving the fit to the observation. However, the well-known trade-off between the attenuation parameters might still limit the source parameter estimation, (e.g., Shible *et al.*, 2022). These issues, as well as a comparison of different spectral fitting techniques on synthetic data, are deserving attention for future studies.

DATA AND RESOURCES

The synthetic data used in this article have been calculated using the procedure outlined by Wang (1999). The seismic noise trace added to the synthetic seismograms was obtained from the Sistema di Monitoraggio terrestre dell'Italia Nord Orientale (SMINO) network (Bragato *et al.*, 2021). The figures were drawn using the Generic Mapping Tools (GMT; Wessel *et al.*, 2019) software.

DECLARATION OF COMPETING INTERESTS

The authors declare that there are no conflicts of interest recorded.

ACKNOWLEDGMENTS

The authors thank the associate editor, Arben Pitarka, as well as Colin Pennington and an anonymous reviewer whose constructive comments helped to improve the article.

REFERENCES

Anderson, J. G. (1986). Implication of attenuation for studies of the earthquake source, in *Earthquake Source Mechanics*, S. Das and J. Boatwright (Editors), American Geophysical Union, Washington, D.C., 311–318.

Bethmann, F., N. Deichmann, and P. M. Mai (2012). Seismic wave attenuation from borehole and surface records in the top 2.5 km beneath the city of Basel, Switzerland, *Geophys. J. Int.* **190,** 1257–1270, doi: 10.1111/j.1365-246X.2012.05555.x.

Blanke, A., G. Kwiatek, T. H. W. Goebel, M. Bohnhoff, and G. Dresen (2021). Stress drop–magnitude dependence of acoustic emissions during laboratory stick-slip, *Geophys. J. Int.* **224,** no. 2, 1371–1380, doi: 10.1093/gji/ggaa524.

Boore, D. M. (1986). The effect of finite bandwidth on seismic scaling relationships, in *Earthquake Source Mechanics*, S. Das and J. Boatwright (Editors), American Geophysical Union, Washington, D.C., 275–283.

Bragato, P. L., P. Comelli, A. Saraò, D. Zuliani, L. Moratto, V. Poggi, G. Rossi, C. Scaini, M. Sugan, C. Barnaba, *et al.* (2021). The OGS–Northeastern Italy seismic and deformation network: Current status and outlook, *Seismol. Res. Lett.* **92,** no. 3, 1704–1716, doi: 10.1785/0220200372.

Brown, M. R. M., and S. Ge (2018). Small earthquakes matter in injection-induced seismicity, *Geophys. Res. Lett.* **45,** no. 11, 5445–5453, doi: 10.1029/2018gl077472.

Brune, J. N (1970). Tectonic stress and the spectra of the seismic shear waves from earthquakes, *Geophys. Res. Lett.* **75,** 4997–5009.

Brune, J. N. (1971). Correction, *J. Geophys. Res.* **76,** no. 20, 5002.

Buijze, L., L. van Bijsterveldt, H. Cremer, B. Paap, H. Veldkamp, B. B. T. Wassing, J.-D. van Wees, G. C. N. van Yperen, J. H. ter Heege, and B. Jaarsma (2019). Review of induced seismicity in geothermal systems worldwide and implications for geothermal systems in the Netherlands, *Neth. J. Geosci.* **98,** e13, doi: 10.1017/njg.2019.6.

Castro, R. R., J. G. Anderson, and S. K. Singh (1990). Site response, attenuation and source spectra of S waves along the Guerrero, Mexico, subduction zone, *Bull. Seismol. Soc. Am.* **80,** no. 6A, 1481–1503.

Chen, X., and R. E. Abercrombie (2020). Improved approach for stress drop estimation and its application to an induced earthquake sequence in Oklahoma, *Geophys. J. Int.* **223,** no. 1, 233–253, doi: 10.1093/gji/ggaa316.

Drouet, S., S. Chevrot, F. Cotton, and A. Souriau (2008). Simultaneous inversion of source spectra, attenuation parameters, and site responses: Application to the data of the French accelerometric network, *Bull. Seismol. Soc. Am.* **98,** no. 1, 198–219, doi: 10.1785/0120060215.

Foulger, G. R., M. P. Wilson, J. G. Gluyas, B. R. Julian, and R. J. Davies (2018). Global review of human-induced earthquakes, *Earth Sci. Rev.* **178,** 438–514, doi: 10.1016/j.earscirev.2017.07.008.

Goertz-Allmann, B. P., A. Goertz, and S. Wiemer (2011). Stress drop variations of induced earthquakes at the Basel geothermal site, *Geophys. Res. Lett.* **38,** no. 9, doi: 10.1029/2011gl047498.

Hanks, T. C., and H. Kanamori (1979). A moment magnitude scale, *J. Geophys. Res.* **84,** no. B5, 2348–2350.

Huang, Y., L. D. Barros, and F. Cappa (2019). Illuminating the rupturing of microseismic sources in an injection-induced earthquake experiment, *Geophys. Res. Lett.* **46,** no. 16, 9563–9572, doi: 10.1029/2019gl083856.

Ide, S., G. C. Beroza, S. G. Prejean, and W. L. Ellsworth (2003). Apparent break in earthquake scaling due to path and site effects on deep borehole recordings, *J. Geophys. Res.* **108,** no. B5, 2271–2287, doi: 10.1029/2001jb001617.

Imperatori, W., and P. M. Mai (2012). Sensitivity of broad-band simulations to earthquake source and Earth structure variations: An application to the Messina Straits (Italy), *Geophys. J. Int.* **188,** 1103–1116, doi: 10.1111/j.1365-246X.2011.05296.x.

Jost, M. L., T. Busselberg, O. Jost, and H. P. Harjes (1998). Source parameters of injection-induced microearthquakes at 9 km depth at the KTB deep drilling site, Germany, *Bull. Seismol. Soc. Am.* **88,** no. 3, 815–832.

Klinger, A. G., and M. J. Werner (2022). Stress drops of hydraulic fracturing induced microseismicity in the Horn River basin: Challenges at high frequencies recorded by borehole geophones, *Geophys. J. Int.* **228,** no. 3, 2018–2037, doi: 10.1093/gji/ggab458.

Ko, Y., B. Kuo, and S. Hung (2012). Robust determination of earthquake source parameters and mantle attenuation, *J. Geophys. Res.* **117,** no. B4, doi: 10.1029/2011jb008759.

Kwiatek, G., F. Bulut, M. Bohnhoff, and G. Dresen (2014). High-resolution analysis of seismicity induced at Berlín geothermal field, El Salvador, *Geothermics* **52,** 98–111, doi: 10.1016/j.geothermics.2013.09.008.

Menke, W., and R. Chen (1984). Numerical studies of the coda falloff rate of multiply scattered waves in randomly layered media, *Bull. Seismol. Soc. Am.* **74,** 1605–1621.

Moratto, L., M. A. Romano, G. Laurenzano, S. Colombelli, E. Priolo, A. Zollo, A. Saraò, and M. Picozzi (2019). Source parameter analysis of microearthquakes recorded around the underground gas storage in the Montello-Collalto Area (Southeastern Alps, Italy), *Tectonophysics* **762,** 159–168, doi: 10.1016/j.tecto.2019.04.030.

Parolai, S. (2018). $\kappa 0$: Origin and usability, *Bull. Seismol. Soc. Am.* **108,** no. 6, 3446–3456, doi: 10.1785/0120180135.

Parolai, S., C. G. Lai, I. Dreossi, O.-J. Ktenidou, and A. Yong (2022). A review of near-surface QS estimation methods using active and passive sources, *J. Seismol.* doi: 10.1007/s10950-021-10066-5.

Pennington, C. N., X. Chen, R.E. Abercrombie, and Q. Wu (2021). Cross validation of stress drop estimates and interpretations for the 2011 Prague, OK, earthquake sequence using multiple methods, *J. Geophys. Res.* **126,** doi: 10.1029/2020JB020888.

Picozzi, M., A. Oth, S. Parolai, D. Bindi, G. D. Landro, and O. Amoroso (2017). Accurate estimation of seismic source parameters of induced seismicity by a combined approach of generalized inversion and genetic algorithm: Application to The Geysers geothermal area, California, *J. Geophys. Res.* **122,** no. 5, 3916–3933, doi: 10.1002/2016jb013690.

Pitarka, A., and R. Mellors (2021). Using dense array waveform correlations to build a velocity model with stochastic variability, *Bull. Seismol. Soc. Am.* **111,** 2021–2041, doi: 10.1785/0120200206.

Raub, C., M. Bohnhoff, B. Petrovic, S. Parolai, P. Malin, K. Yanik, R. F. Kartal, and T. Kiliç(2016). Seismic-wave propagation in shallow layers at the GONAF-Tuzla Site, Istanbul, Turkey, *Bull. Seismol. Soc. Am.* **106,** no. 3, 912–927, doi: 10.1785/0120150216.

Schultz, R., R. J. Skoumal, M. R. Brudzinski, D. Eaton, B. Baptie, and W. Ellsworth (2020). Hydraulic fracturing-induced seismicity, *Rev. Geophys.* **58,** no. 3, e2019rg000695, doi: 10.1029/2019rg000695.

Shible, H., F. Hollender, D. Bindi, P. Traversa, A. Oth, B. Edwards, P. Klin, H. Kawase, I. Grendas, R. R. Castro, *et al.* (2022). GITEC: A generalized inversion technique benchmark, *Bull. Seismol. Soc. Am.* **112,** 850–877, doi: 10.1785/0120210242.

Supino, M., G. Festa, and A. Zollo (2019). A probabilistic method for the estimation of earthquake source parameters from spectral inversion: Application to the 2016–2017 Central Italy seismic sequence, *Geophys. J. Int.* **218,** no. 2, 988–1007, doi: 10.1093/gji/ggz206.

Wang, R. (1999). A simple orthonormalization method for stable and efficient computation of Green's functions, *Bull. Seismol. Soc. Am.* **89,** no. 3, 733–741.

Wessel, P., J. F. Luis, L. Uieda, R. Scharroo, F. Wobbe, W. H. F. Smith, and D. Tian (2019). The generic mapping tools version 6, *Geochem. Geophys. Geosys.* **20,** 5556–5564, doi: 10.1029/2019GC008515.

Wu, R.-S., and K. Aki (1988). Introduction: Seismic wave scattering in three-dimensionally heterogeneous earth, *Pure Appl. Geophys.* **128,** nos. 1/2, 1–6, doi: 10.1007/bf01772587.

Zollo, A., A. Orefice, and V. Convertito (2014). Source parameter scaling and radiation efficiency of microearthquakes along the Irpinia fault zone in southern Apennines, Italy, *J. Geophys. Res.* **119,** no. 4, 3256–3275, doi: 10.1002/2013jb010116.

Manuscript received 3 April 2022
Published online 29 July 2022